Electromagnetic Characteristics in Radial Flux Permanent Magnet BLDC Motor for Light Electric Vehicle Application

A. Paramasivan[1], M. L. Mohd Jamil[1,2*], A. Jidin[1,2*]
[1]EV-PRODRIVES Research Group, [2]Department of Electrical Engineering, Faculty of Electrical Technology and Engineering, Universiti Teknikal Malaysia Melaka, Hang Tuah Jaya, 76100 Durian Tunggal, Melaka, Malaysia
*corresponding author's email: luqman@utem.edu.my

Abstract – *This research work investigates electromagnetic characteristics and evaluates the performance of fractional-slot radial flux permanent magnet (RFPM) motors, 12-slot and 9-slot stators combined with an identical 10-pole rotor for a light electric vehicle system application. At design stage, key parameters such as output power, output torque, speed, voltage supply, outer diameter and axial length are fixed to meet a lightweight vehicle design concept. The electromagnetic characteristics, such as open-circuit flux density, phase back-emf and output torque, are calculated using finite element analysis (FEA) and subsequently verified by a 1-D analytical model. Both results deduced from the FEA and analytical model show a good agreement between them. From the FEA results, the 12-slot motor produced a higher average torque than the 9-slot motor under both static and dynamic conditions. Under ideal trapezoidal current excitation (static condition), the 9-slot motor exhibited a smoother torque profile with lower torque ripple, owing to its lower cogging torque. Under inverter-fed operation (dynamic condition), however, the 12-slot motor exhibited lower torque ripple, mainly because the asymmetrical phase-winding distribution of the 9-slot motor intensifies commutation torque ripple. As the dynamic condition better represents a practical motor drive system, the 12-slot/10-pole configuration is found to be more suitable for the LEV application.*

Keywords: *FEA, Light Electric Vehicle, RFPM; Slot/pole combination; Torque;*

Article History
Received 31 August 2026
Received in revised form 17 September 2026
Accepted 24 September 2026
Published online October 2026

I. Introduction

The global shift toward environmental sustainability has accelerated the transition from internal combustion engine (ICE) vehicles to electric vehicles (EVs) [1]. While conventional ICE vehicles generate substantial greenhouse gas emissions and environmental noise, EVs offer a low-emission, low-noise alternative with distinct environmental benefits for densely populated urban centers [2]. At the core of this transition is the electric propulsion system, where the design and performance of the electric motor not only dictate vehicle dynamics but also directly influence government-mandated sustainability targets [3].

As various electric machine technologies exist, their adoption depends heavily on specific operational demands. Historically, induction motors have been favored in industrial applications for their mechanical simplicity and durability [4], whereas permanent magnet synchronous motors (PMSMs) dominate high-performance applications due to their exceptional efficiency and dynamic responsiveness [5]. Similarly, switched reluctance motors (SRMs) are gaining traction for EV integration due to their robust rotor structures and inherent fault tolerance [6]. However, for compact and highly controllable systems, brushless DC (BLDC) motors have emerged as a premier choice for EV propulsion [7]. Among these technologies, BLDC motors are uniquely suited for electric transport due to their superior efficiency, high torque density, and precise electronic controllability [8]. By replacing mechanical brushes with a six-step electronic commutation sequence, BLDC motors eliminate brush-wear maintenance, significantly enhancing operational reliability [9]. Furthermore, their exceptional torque-to-rotor volume (TRV) ratio yields a compact physical footprint, making

This is an Open Access article distributed under the terms of the Creative Commons Attribution 4.0 International License, permitting copy and redistribution of the material and adaptation for commercial and uncommercial use.

them ideal for space-constrained configurations such as in-wheel hub drives without sacrificing torque output [10]. This compact architecture minimizes copper and iron losses crucial for maximizing the range of battery-powered systems [11], while the integration of flux-weakening control extends the motor's operational speed range across diverse driving conditions [12]. Although mainstream EV research frequently prioritizes high-power passenger vehicles, lightweight electric vehicles (LEVs) represent a highly practical and rapidly expanding segment of sustainable urban transit [13]. LEVs, including electric scooters, mopeds, and bicycles, are widely adopted globally due to their affordability, small footprint, and urban utility [14]. Market projections indicate the global LEV sector will reach USD 135.65 billion by 2029, while the e-bike market alone is expected to expand to USD 113.64 billion by 2030 [15]. This shift aligns with localized de-carbonization frameworks, such as Malaysia's National Energy Transition Roadmap (NETR), which advocates for transport electrification to meet national emissions targets. To optimize the utility of LEVs, engineering efforts must target their core propulsion systems. A comparative analysis of electric machines with different flux orientations was presented in [16], [17], highlighting a trade-off among electromagnetic performance, design and analysis complexity, and manufacturing requirements. Although axial-flux machines can offer superior performance in terms of torque density and compactness, their relatively complex electromagnetic design, analysis, and manufacturing processes may limit their suitability for low-cost LEV applications. For instance, a high-power-density axial-flux motor developed for an electric bike required the stator tooth tips to be removed to simplify the core shape, together with additional magnetic sensors to fit the tight housing, illustrating the manufacturing constraints associated with this topology [18]. Therefore, the radial-flux motor topology is considered a more practical option for cost-sensitive LEV development. Recent studies on radial-flux machines for light electric mobility support this direction. Ozer and Yilmaz [19] optimized an interior PM synchronous motor for a commercial two-wheeled cargo LEV and reported a 13% reduction in motor cost, a 12% reduction in magnet usage and a 1.4% improvement in efficiency compared with the commercial motor. Naeimi et al. [20] proposed an external-rotor consequent-pole PM machine for in-hub e-bikes that increased PM utilization by 80.4% and reduced PM cost by about 50% relative to a surface-mounted PM machine, while also achieving the lowest cogging torque among the compared designs. For in-wheel drives, Wang et al. [21] showed that the rotor arrangement of a fractional-slot PM machine strongly influences the average torque, field-weakening capability and high-efficiency region under a constrained machine diameter. Nevertheless, torque ripple and acoustic noise remain key challenges in BLDC drives [22], and most of these studies focus on rotor topology or magnet arrangement rather than on the influence of the stator slot number under an identical rotor. Within radial-flux BLDC machines, the fractional-slot winding configuration provides considerable flexibility in selecting the slot and pole numbers, while simultaneously influencing the coil distribution and electromagnetic characteristics of each phase.

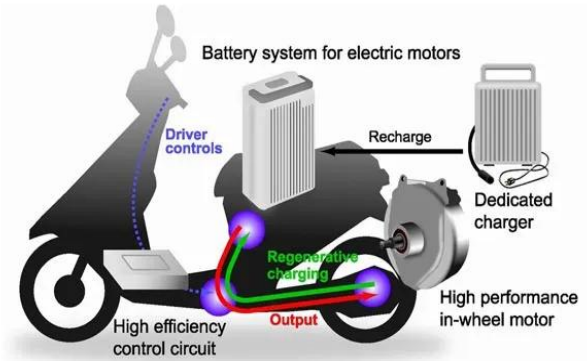
Despite the extensive use of fractional-slot windings in BLDC machines, the influence of different slot configurations on the overall electromagnetic performance remains an important design consideration, particularly for low-cost LEV applications. In particular, a direct comparison between the 12-slot/10-pole and 9-slot/10-pole fractional-slot BLDC configurations under identical rotor dimensions and operating constraints has not been sufficiently established. Differences in slot number and winding distribution can significantly affect the back-EMF waveform, average output torque, torque ripple, and cogging torque, which are critical factors determining motor smoothness, efficiency, acoustic behavior, and driving performance in lightweight electric mobility.

Accordingly, this study investigates and compares the electromagnetic performance of 12-slot/10-pole and 9-slot/10-pole fractional-slot BLDC motors employing an identical rotor structure and subjected to the same design constraints in terms of power rating, dimensional envelope, speed, and operating conditions. The comparison focuses specifically on the back-EMF waveform and magnitude, average output torque, torque ripple, and cogging torque to identify the more suitable slot configuration for low-cost LEV applications as illustrated in Fig. 1 [23]. Fig. 1(a) shows a typical two-wheeler electric scooter comprising a battery system with a dedicated charger, driver controls, a control circuit and an in-wheel motor, while Fig. 1(b) represents the same system as a drive block scheme, in which a power converter regulated by the controller links the battery to the in-wheel motor and adjusts the current supplied to it according to the driver demand. Moreover, the study in [24] identified permanent magnet synchronous motors as the most suitable traction motors for e-bikes and analysed a commercial 12-slot/10-pole spoke-type PM motor through FEA and experimental tests. The comparative investigation is conducted using finite element analysis (FEA), with the results subsequently verified against a one-dimensional (1-D) analytical model. The FEA–analytical correlation is an important aspect of this study because it not only validates the proposed motor designs but also establishes the reliability and practical

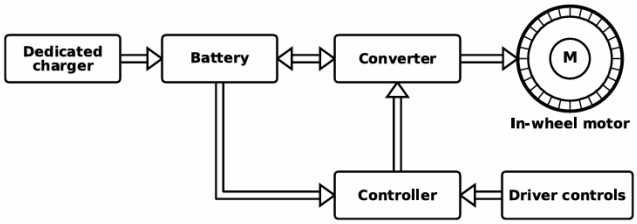
applicability of a simplified analytical design approach. Once a satisfactory level of agreement between the 1-D analytical solution and FEA results is demonstrated, the analytical model can be used as an efficient preliminary design and screening tool before detailed work such as numerical optimization. This approach has the potential to reduce the dependence on sophisticated and costly commercial FEA software, particularly during the early stages of low-cost BLDC motor development. Hence, the study contributes not only to the identification of a more appropriate fractional-slot configuration for LEV applications, but also to the development of a computationally efficient and economically attractive motor design methodology.

II. Design and Estimation Approach

The development of the BLDC motor for lightweight electric vehicle applications is illustrated in Fig. 2. Initially, the required motor power and operating speed are determined through vehicle dynamic calculations to satisfy the intended driving requirements. The motor dimensions are then fixed in terms of the outer diameter



(a) Two-wheeler lightweight motor [23]



(b) Basic drives system

Fig. 1. LEV application drives system

and axial length to ensure the motor will fit within the available installation space, followed by the selection of

the appropriate slot/pole combination, and preliminary sizing. This stage covers stator and rotor geometry design, winding arrangements and coil layouts, leading to initial electromagnetic simulations. Parametric optimization is subsequently performed by refining the magnet thickness, tooth geometry, and back-iron dimensions while maintaining the specified outer dimension. The optimized design is then evaluated using FEA, employing adaptive automatic meshing with element-length refinement to improve solution accuracy in regions with high magnetic field gradients. Meshing is applied only to the defined computational domains, including the stator, rotor, permanent magnets, windings, air-gap, and surrounding air regions, while a rotating boundary condition is assigned to the rotor to simulate continuous operation. The electromagnetic characteristics predicted by FEA are subsequently verified using the developed analytical model through comparison of the flux density, phase back-emf and electromagnetic torque.

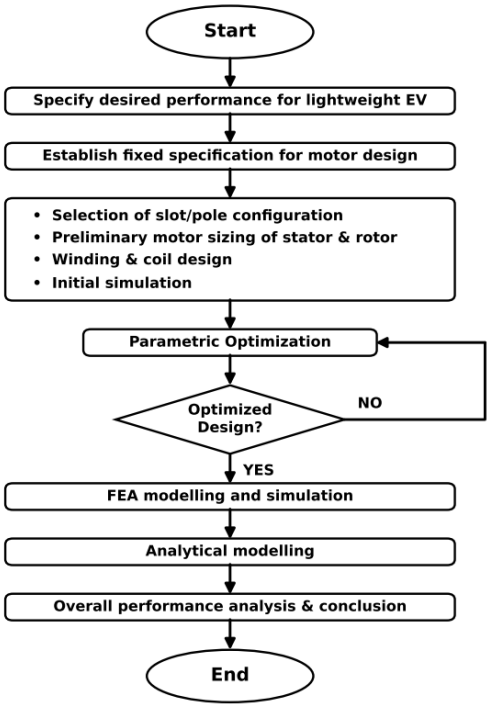


Fig. 2. Design flowchart

A. Vehicle Dynamics Calculation

To determine the motor's required performance specifications, a basic vehicle dynamics analysis is conducted based on typical parameters of a lightweight electric scooter. The key values used in this analysis are listed in Table I.

TABLE I
VEHICLE DYNAMICS OF LIGHTWEIGHT ELECTRIC SCOOTER

Parameter	Values
Tyre outer diameter	215 mm
Overall mass	150 kg
Maximum speed	35 km/h
Tyre size	8.5 inch
Power train system	Direct-drives

By analysing a scooter and rider whose combined weight is 150 kg and a tire outer diameter of 8.5 inches (which is 215 mm), achieving a top speed of 35 km/h on a level road corresponds to a wheel speed, n, of approximately 864 rpm, while climbing a 4.5° slope at about 18 km/h corresponds to 450 rpm. Eq. (1) represents the fundamental calculation for n;

$$n = (km/h)/ (0.1885 \times Wheel\ Outer\ Diameter) \quad (1)$$

Since the direct-drive motor must deliver its highest torque when climbing, the slope condition (450 rpm) is taken as the rated operating point. The total force, F_{Total} required to drive the scooter at the rated speed of 450 rpm is the sum of the rolling resistance, $F_{rolling}$, gradient resistance, $F_{gradient}$, and aerodynamic drag, F_{drag} that calculated by using Eq. (2) [25].

$$F_{Total} = F_{rolling} + F_{gradient} + F_{drag} \quad (2)$$

Table II tabulates parameters used for calculating the required force to move the scooter.

TABLE II
PARAMETERS FOR CALCULATION OF F_{TOTAL}

Parameter	Values
Coefficient of Rolling Resistance	0.004
Total mass, M	150 kg
Gravitational constant, g	9.81 m/s²
Inclination angle, θ	4.5°
Drag coefficient, C_D	0.6
Frontal area, A_F	0.8 m²
Air density, ρ	1.1644 kg/m³
Rated speed, n	450 rpm

$F_{rolling}$ is the force that opposes the motion of the scooter due to the contact between the tires and the ground. It is calculated using the coefficient of rolling resistance C_{rr}, the total mass, M, and the acceleration due to gravity g shown in Eq. (3) [25].

$$F_{rolling} = C_{rr} \times M \times \mathrm{g} \quad (3)$$

$F_{gradient}$, is the force required to move the scooter up an incline. It is calculated using the mass , M, gravity, g, and the sine of the incline angle, θ.

$$F_{gradient} = M \times g \times \sin(\theta) \quad (4)$$

F_{drag} is the resistance faced by the scooter due to air while moving. It is calculated using the drag coefficient, C_D, frontal area, A_F , air density, ρ, and the square of the velocity, v.

$$F_{drag} = 0.5 \times C_D \times A_F \times \rho \times v^2 \quad (5)$$

From the calculated F_{total}, the output power, P_o and rated torque, τ as in Eq. (6) and (7) are determined to ensure the motor meets the required performance based on electric scooter specification. Table III compares the findings for the scooter in flat road and inclined road conditions. The flat-road values in Table III are rounded up from the calculated values (864 rpm, 314 W and 3.5 Nm) to include a design margin; however, is governed by the slope condition.

$$P_o = F_{Total} \times v \quad (6)$$

$$\tau = \frac{60 \times P_o}{2\pi \times n} \quad (7)$$

TABLE III
ROAD CONDITIONS

	Flat Road	Slope road (θ=4.5°)
Output power, P_o	350 W	650 W
Speed, n	900 rpm	450 rpm
Torque, τ	3.7 Nm	13.8 Nm

B. Motor sizing and dimension

Lightweight electric scooters commonly use 8.5-inch tires, which typically have an inner diameter of about 140 mm and a width of 50 mm. To fit within this space, the motor is designed with an outer diameter of 120 mm and an active stator length of 20 mm for stator and rotor. This forms the electromagnetic design region, excluding end-winding overhang. When the end windings are considered, the total axial length extends to 48 mm. Table IV tabulates main specification for the proposed motor. It should be mentioned a maximum output power of 650W (slope road of 4.5°) is assumed constant, even as torque and speed vary inversely with each other leading constant motor efficiency.

TABLE IV
MAIN MOTOR SPECIFICATIONS

Parameter	Values
Output power, P_o	650 W
Speed, n	450 rpm
Torque, τ	13.8 Nm
Outer diameter, D_s	120 mm
Axial length, l_a	20 mm
Phase number, m	3
DC supply, V_s	48 V

Theoretically, initial dimensions of magnetic segments are calculated based on the desired magnetic flux within the motor's magnetic circuit. The magnetic flux is assumed to follow a defined path, and each section of this path is assigned a target flux density, as summarized in Table V. These values, typically in the range of 0.8 T to 1.8 T depending on the region of the motor. The sizing of each magnetic segment proportionally prevents saturation and ensure efficient flux linkage. Using the specified flux densities, the initial dimensions including the stator tooth width, T_w, the tooth tip width, T_{tw}, and the stator back iron thickness, L_{sbi}, are calculated through Eq.

(8) to (10). Where, R_s is the stator inner radius, W_{so} is the stator slot opening θ_s is slot pitch in radian. and N_s is the stator number of slots. These equations relate the magnetic flux and flux density to the cross-sectional area of each component, allowing the necessary sizing for each magnetic region to support the expected magnetic loading. This ensures that the magnetic path is properly dimensioned to support the required flux without exceeding material saturation limits.

TABLE V
PREDICTED FLUX DENSITY

Magnetic segments	Flux density (T)
Stator back iron, B_{sbi}	1.2
Stator tooth, B_{st}	1.8
Tooth-tip, B_{tt}	0.9
Rotor back iron, B_{rbi}	1.4

$$T_w = \frac{B_{tt}}{B_{st}} \times T_{tw} \quad (8)$$

$$T_{tw} = \theta_s R_s - W_{so} \quad (9)$$

$$L_{sbi} = \frac{B_{st}}{B_{sbi}} \times T_w \quad (10)$$

The tooth-tip thickness, slot chamfer height, and slot radius are selected to ensure minimal reduction of effective slot depth. The slot depth is influenced by the split ratio of the motor, defined as the ratio of rotor outer diameter to stator outer diameter. For radial flux machines, an optimal split ratio typically falls within the range of 0.6 to 0.7, balancing between magnetic performance and mechanical strength [26]. Similar to the stator back iron, the rotor back iron thickness is determined using Eq. (11), based on the required magnetic flux and allowable flux density to prevent saturation.

$$L_{rbi} = \frac{B_{st}}{B_{rbi}} \times T_w \quad (11)$$

An accurate calculation of end winding length is essential for an optimal stator casing size. For an internal rotor motor, the end winding length, l_e can be approximated as a half-circle spanning one slot pitch and the effective stator axial length, l_a are expressed as in Eqn. (12) and (13).

$$l_e = \frac{\pi(D_s - 2L_{sbi})}{2N_s} \quad (12)$$

$$l_a = l_s + 2l_e \quad (13)$$

The 12-slot/10-pole and 9-slot/10-pole configurations were selected because they provide relatively high winding factors of 0.933 and 0.945, respectively, resulting in efficient torque production while maintaining compact concentrated windings suitable for lightweight electric vehicle applications [27]. The even and odd stator slot configurations enable a direct comparison of slot/pole combinations on harmonic content, cogging torque, back-EMF characteristics, torque ripple, and overall electromagnetic performance. Table VI summarizes the design specifications. The axial length of both motors is kept identical in this study to ensure a fair comparison and allow both motors to share the same rotor design. Additionally, the number of turns and conductor size, which directly affect the slot fill factor, are determined using FEA.

TABLE VI
DESIGN SPECIFICATIONS

Parameter	Values	
	(N_s = 12)	(N_s = 9)
DC supply, V_s	48 V	
Rated speed, ω_r	450 rpm	
Rated power, P_o	650 W	
Air gap thickness, l_g	1 mm	
Slot number, N_s	12 , 9	
Stator outer diameter, D_s	120 mm	
Stator inner diameter, D_{si}	74 mm	
Split ratio, λ	0.6167	
Stator slot opening, W_{so}	3 mm	
Stator tooth width, T_w	8.4 mm	11.6 mm
Stator back iron thickness, L_{sbi}	6.3 mm	8.7 mm
Tooth tip width, T_{tw}	2 mm	
Slot base fillet radius, r_{sb}	0.5 mm	
Slot chamfer height, T_{sc}	1 mm	
Slot depth, T_s	13.7 mm	10.3 mm
Stator axial length, l_s	20 mm	
Coil turn numbers, N_{coil}	60	66
Pole numbers, $2p$	10	
Pole embrace	1	
Rotor outer diameter, D_{ro}	72 mm	
Rotor inner diameter, D_{ri}	48.8 mm	
Rotor back iron thickness, L_{rbi}	6.6 mm	
Magnet thickness, l_m	5 mm	
Rotor axial length, l_r	20 mm	
Ferromagnetic material	M250-35A	
Magnet type	NdFeB (N35)	

Fig. 3 compares the design layout for both motors. It is observable that the 12-slot motor's coil distribution for each phase is symmetrically positioned, whereas the 9-slot motor has an asymmetric form.

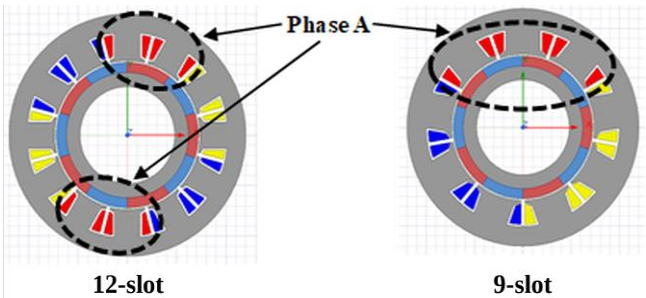


Fig. 3. 12-slot & 9-slot basic motor design layout

C. Analytical model

For a comparison, the motor performance is also calculated using 1-D analytical model [26], [28]. In summary, Eqs. (14), (15) and (16) represent open-circuit flux density, phase back-emfs in the 12-slot motor and phase-emfs in the 9-slot motor, respectively.

$$B_{o/c}(\theta_e) = \sum_n B_n \cos(np\theta_e) \tag{14}$$

$$emf_{ph-12} = 2R_s l_s N_{ph} \omega_r \sum_n B_n K_{wn} \times sin[np\omega_r t + \left(\frac{\pi}{2} - \frac{np\pi}{N_s}\right)] \tag{15}$$

$$emf_{ph-9} = 2R_s l_s N_{ph} \omega_r \sum_n B_n K_{wn} \, sin(np\omega_r t) \tag{16}$$

where θ_e, R_s, l_s, N_{ph}, ω_r, t, p, n, B_n, K_{wn}, and N_s are the electrical angle, tooth-tip radius, stator axial length, number of turns per phase, rotor speed, time, pole pair number, harmonic order, radial component harmonics of magnetic field, winding factor and slot number respectively. The electromagnetic torque is then expressed as;

$$T_{em} = \frac{emf_{pha} I_a + emf_{phb} I_b + emf_{phc} I_c}{\omega_r} \tag{17}$$

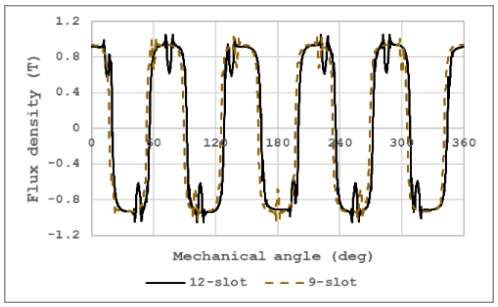
where emf_{pha}, emf_{phb}, emf_{phc}, I_a, I_b, and I_c are the phase back-emf of phase a, phase back-emf of phase b, phase back-emf of phase c, current in phase a, current in phase b and current in phase c respectively.

III. Result and Discussion

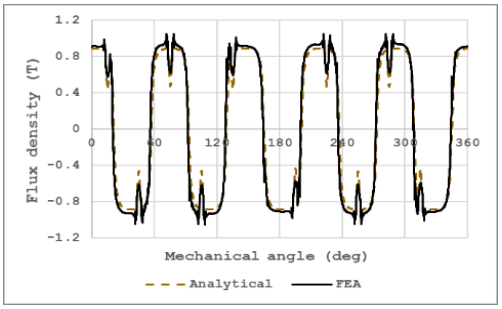
A set of comparison of predicted results between FEA simulation and analytical methods is presented.

A. Open-circuit flux density

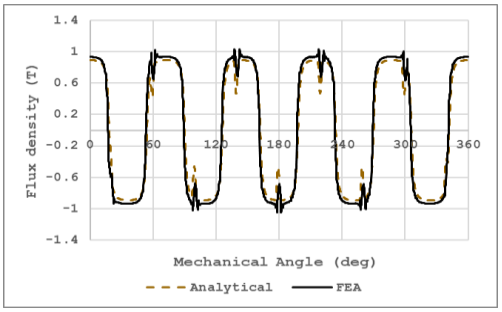
Open-circuit flux density waveforms for the 12-slot and 9-slot motor configurations are presented in Fig. 4. As shown in Fig. 4 (a), the FEA-predicted flux densities exhibit peak values of approximately 0.85 T. Notably, minor dents at the peak of each positive and negative half-cycle are evident, resulting from the effect of slot openings on the magnetic field distribution. Fig. 4(b) and 4(c) provide a comparative analysis between FEA and analytical predictions, demonstrating strong agreement between both approaches. Furthermore, the observed reduction in flux density near the slot regions in both models confirms that the analytical formulation effectively accounts for the stator slotting effect. This alignment validates the accuracy of the analytical method in capturing the essential electromagnetic behaviour of the motor. Moreover, Fig. 4 (d) and (e) illustrate the magnetic flux distribution (flux contour) of the 12-slot and 9-slot configurations, respectively. The flux distribution plots represent an instantaneous magnetic field condition at a specific rotor position during open-circuit operation, providing a snapshot of the magnetic flux paths within the motor. In both models, the magnetic flux is symmetrically distributed throughout the stator, indicating balanced magnetic loading and effective flux linkage. Higher flux concentration is observed around the stator tooth and air gap region due to the magnetic path established between the permanent magnets and stator teeth. The 12-slot configuration exhibits a slightly more uniform flux distribution pattern, while the 9-slot configuration shows relatively higher flux concentration at certain tooth regions due to the reduced slot number. Nevertheless, both configurations maintain smooth magnetic flux paths without severe saturation, demonstrating effective electromagnetic performance.



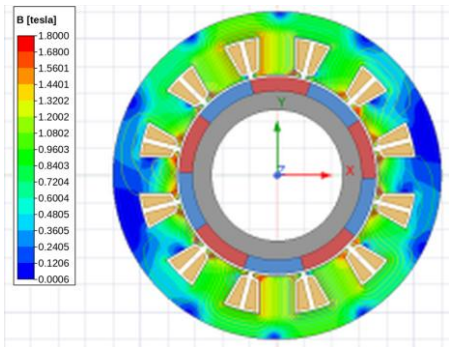
(a) FEA: 12-slot vs 9-slot



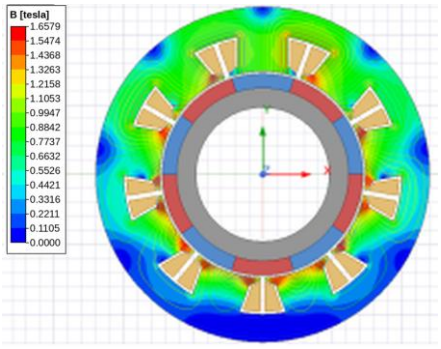
(b) FEA vs Analytical; 12-slot



(c) FEA vs Analytical; 9-slot



(d) Flux contour; 12-slot

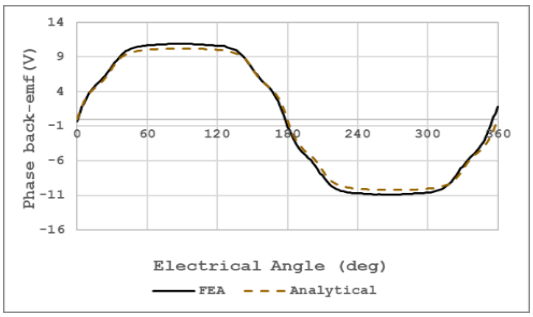


(e) Flux contour; 9-slot

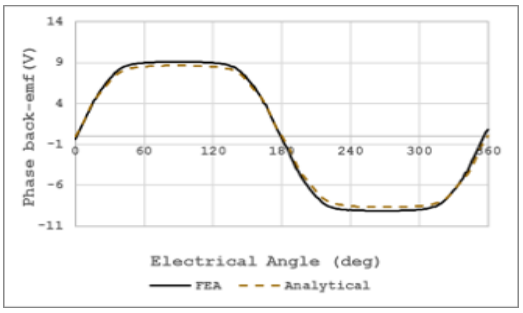
Fig. 4. Open-circuit flux densities

B. Phase back-emf

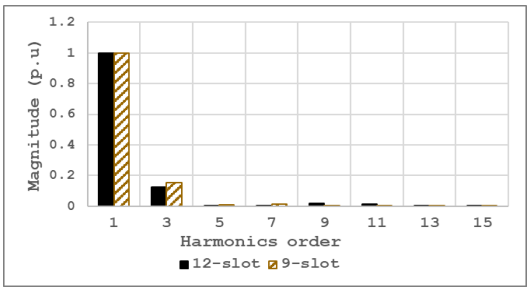
Fig. 5 presents the phase back-emf obtained through both FEA and analytical methods. A good agreement between both methods is achieved showing that the analytical method provides a reliable prediction. Both motors exhibit a non-sinusoidal profile, characterized by concentrated winding configurations and the harmonic characteristics. Notably, the 9-slot motor exhibits a slightly higher amplitude in the 3rd harmonic compared to the 12-slot motor, contributing to a more trapezoidal waveform. Table VII summarizes the RMS values of the phase back-emf.



(a) FEA vs Analytical; 12-slot



(b) FEA vs Analytical; 9-slot



(c) Harmonics spectrum

Fig. 5. Phase back-emf

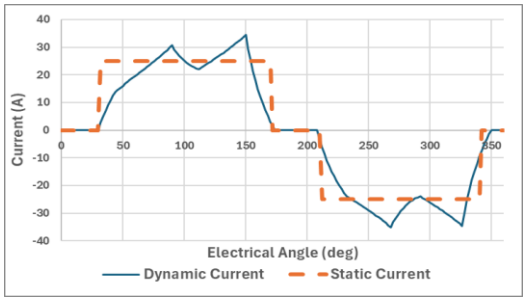
TABLE VII
PREDICTED PHASE BACK-EMF

	Phase back-emf (V)	
	12-slot	9-slot
FEA	8.9	7.6
Analytical	8.6	7.4

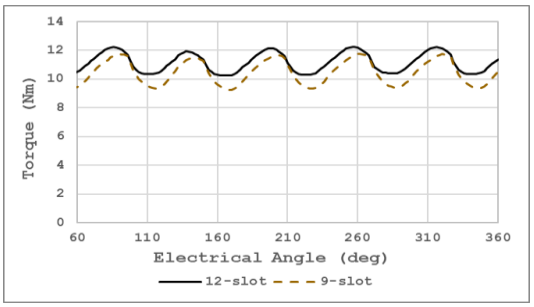
C. Electromagnetic torque

Theoretically, torque production is deduced under an ideal switching condition of 120° commutation process. A trapezoidal current is excited in each phase of BLDC motor as shown Fig. 6 (a), illustrate current excitation in static and dynamic condition where an ideal trapezoidal current belongs to static condition and the one with fishbone shape represents the effect of because phase inductance that resist sudden current changes. Under dynamic condition, the motors are virtually driven using an ideal inverter powered by a 48 V DC bus. In Fig. 6 (b), the output torque profiles of the 12-slot and 9-slot motors operating in BLDC mode with six step commutation are recorded. The average torque for 12-slot and 9-slot motors are 11.2 Nm and 10.4 Nm, respectively. The corresponding peak-to-peak torque variations are approximately 1.9 Nm and 2.5 Nm, with percentage torque ripples of 17.0% and 24.0% for the 12-slot and 9-slot motors, respectively. Instead of commutation effect, the torque ripple is also influenced by the slot/pole combination and slot harmonics leading to a relatively larger cogging torque that deliberately affect the output electromagnetic torque. In Figs. 6 (c), the 12-slot motor produces a slightly higher average torque than the 9-slot motor. However, the 9-slot motor

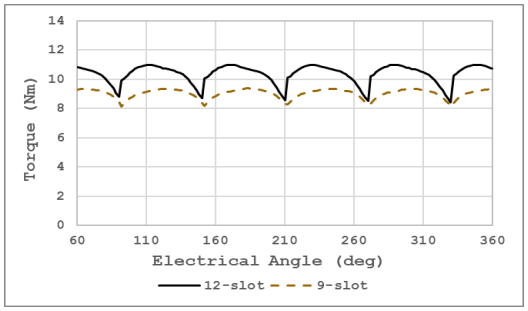
exhibits lower torque ripple in the static FEA results, indicating smoother operation under ideal current excitation. Figs. 6 (d) and (e) compare torque profiles of both motors using the FEA and analytical methods. The analytical model predicts a consistently higher average torque and exhibits a more balanced and symmetric ripple profile, while the FEA method results a slight asymmetric shape. This variation arises due to the assumptions in the analytical model does not incorporate magnetic saturation, and only single operating condition on the magnetic material's B-H curve is used for permeability estimation. In addition, Eq. (17) does not include the cogging torque component; hence, the analytical model underestimates the torque ripple of the 12-slot motor, whose cogging torque is significantly larger, while showing close agreement for the 9-slot motor. Table VIII summarizes the predicted torques.



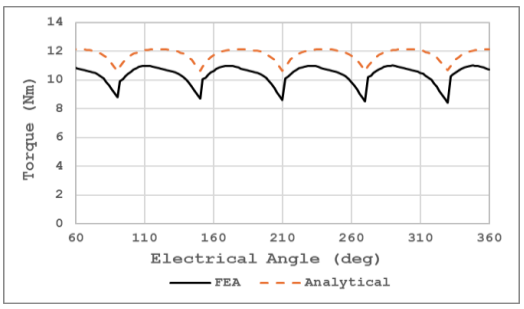
(a) Phase excitation: static vs dynamic



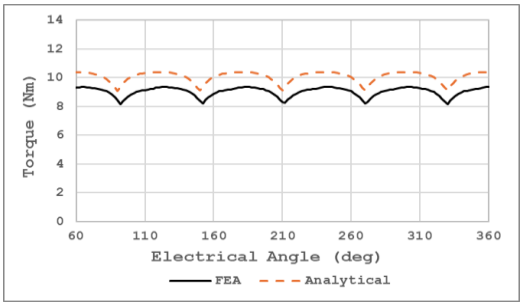
(b) Dynamic condition: 12-slot vs 9-slot



(c) Static condition: 12-slot vs 9-slot



(d) Static condition: FEA vs Analytical (12-slot)



(e) Static condition: FEA vs Analytical (9-slot)

Fig. 6. Electromagnetic torque characteristics

TABLE VIII
OUTPUT TORQUE PERFORMANCE

		12-slot	9-slot
Average torque (Nm)	FEA	10.4	9.0
	Analytical	11.7	10.1
Peak-to-peak torque (Nm)	FEA	3.04	1.06
	Analytical	1.4	1.2
Torque ripple (%)	FEA	29.2	11.7
	Analytical	12.0	12.0

D. Cogging torque

Fig. 7. compares cogging torque in both motors as deduced by the FEA method. The cogging torque arises from the periodic variation in magnetic reluctance due to the interaction between rotor magnets and stator teeth. The 12-slot motor exhibits bigger cogging torque than the 9-slot motor and in contrast, it demonstrates fewer cogging cycles per mechanical revolution than the 9-slot motor. This behaviour is consistent with the slot pole interaction frequency, which is governed by the least common multiple, *Nscm* of the slot/pole combination. In addition, a relation between the cogging torque and the torque ripple exists as there is a correlation between the cogging torque magnitude and the size of torque ripple. Here the 12-slot motor has bigger cogging torque than the 9-slot motor and at the same time it has a bigger torque ripple than the 9-slot motor as summarized in Table VIII (29.2% > 11.7%).

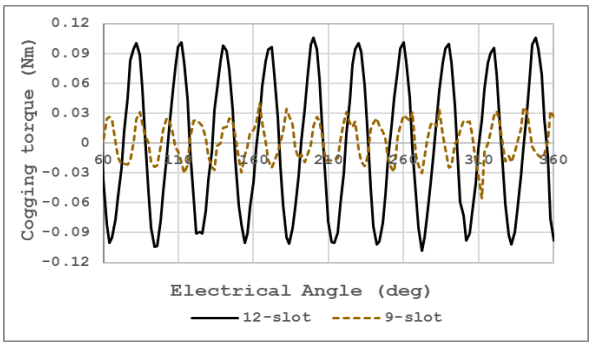


Fig. 7. Cogging torque in 12-slot and 9-slot motors

IV. Conclusion

This paper presented the design and electromagnetic performance comparison of three-phase 12-slot/10-pole and 9-slot/10-pole RFPM motors for LEV application, which is limited to electromagnetic analysis only. The motor specifications were first determined from vehicle dynamics analysis, followed by FEA to evaluate the electromagnetic performance of both configurations under the same design constraints. The FEA results showed good agreement with the 1-D analytical model in terms of open-circuit flux density, phase back-EMF, and output torque. The small difference in torque prediction was mainly caused by the simplified permeability assumption used in the analytical model. The 12-slot/10-pole motor produced a higher average torque under both static and dynamic conditions and a lower torque ripple under dynamic operation, whereas the 9-slot/10-pole motor achieved a lower cogging torque and a lower torque ripple only under static (ideal current) excitation. Considering the torque requirement and the dynamic torque ripple of the LEV, the 12-slot/10-pole motor was found to be more suitable for the compact direct-drive application. The good agreement between the FEA and analytical results also shows that the 1-D model can be used for preliminary motor design and slot/pole selection for a considerable fractional power. This can reduce the need of FEA software during the early design stage and provide a simpler and lower-cost design approach. Future work should investigate the correlation between slot/pole combinations, magnitude of cogging torque and output torque ripple on the unwanted vibration and acoustic noise.

Acknowledgements

The authors wish to acknowledge the Universiti Teknikal Malaysia Melaka, for supporting this research under postgraduate study programme.

Conflict of Interest

The authors declare no conflict of interest in the publication process of the research article.

Author Contributions

Author 1: Data collection, analysis, writing – original draft preparation; Author 2: Supervision, draft review and editing, result investigation and validation; Author 3: Supervision, draft review and editing, result investigation and validation.

References

[1] R. Udendhran et al., "Transitioning to sustainable e-vehicle systems – Global perspectives on the challenges, policies, and opportunities," Journal of Hazardous Materials Advances, vol. 17, p. 100619, Feb. 2025, doi: 10.1016/j.hazadv.2025.100619.

[2] J. D. Tan et al., "Electric vehicle in Malaysia: Power source challenges, infrastructure gaps and international benchmarking," Energy Conversion and Management: X, vol. 28, p. 101307, Oct. 2025, doi: 10.1016/j.ecmx.2025.101307.

[3] S. Kulkarni, "Editorial: Global sustainability: Trends, challenges, and case studies," in Global Sustainability: Trends, Challenges & Case Studies, S. Kulkarni and A. K. Haghi, Eds., World Sustainability Series. Cham, Switzerland: Springer, 2024, pp. 3–17, doi: 10.1007/978-3-031-57456-6_1.

[4] F. J. T. E. Ferreira, G. Baoming, and A. T. de Almeida, "Reliability and operation of high-efficiency induction motors," in Proc. 51st IEEE/IAS Industrial and Commercial Power Systems Technical Conf. (I&CPS), 2015, doi: 10.1109/ICPS.2015.7266412.

[5] M. M. Elkholy, M. M. Algendy, and E. A. El-Hay, "Modern control techniques and operational challenges in permanent magnet synchronous motors: A comprehensive review," Automation, vol. 6, no. 4, p. 49, Sep. 2025, doi: 10.3390/automation6040049.

[6] K. Sreeram, P. K. Preetha, J. Rodríguez-García, and C. Álvarez-Bel, "A comprehensive review of torque and speed control strategies for switched reluctance motor drives," CES Transactions on Electrical Machines and Systems, vol. 9, no. 1, pp. 46–75, Mar. 2025, doi: 10.30941/CESTEMS.2025.00006.

[7] N. Prabhu, R. Thirumalaivasan, and B. Ashok, "Critical review on torque ripple sources and mitigation control strategies of BLDC motors in electric vehicle applications," IEEE Access, vol. 11, pp. 115699–115739, 2023, doi: 10.1109/ACCESS.2023.3324419.

[8] S. Madichetty, S. Mishra, and M. Basu, "New trends in electric motors and selection for electric vehicle propulsion systems," IET Electrical Systems in Transportation, vol. 11, no. 3, pp. 186–199, Sep. 2021, doi: 10.1049/els2.12018.

[9] S. Derammelaere, M. Haemers, J. de Viaene, F. Verbelen, and K. Stockman, "A quantitative comparison between BLDC, PMSM, brushed DC and stepping motor technologies," in Proc. 19th Int. Conf. Electrical Machines and Systems (ICEMS), Chiba, Japan, Nov. 2016.Chiba, Japan, Nov. 2016, pp. 1–5.

[10] S. Jafarishiadeh and M. Amini, "Design and comparison of axial-flux PM BLDC motors for direct drive electric vehicles: Conventional or similar slot and pole combination," International Journal of Engineering Innovation & Research, vol. 6, no. 1, pp. 1–2, 2017.

[11] T. A. Lipo, "A low-loss permanent-magnet brushless DC motor utilizing tape wound amorphous iron," IEEE Trans. Ind.

Appl., vol. 28, no. 3, pp. 646–651, 1992, doi: 10.1109/28.137452.

[12] Z. Feng, R. R. Ramesh, S. Ebrahimi, and J. Jatskeavich, "Flux-weakening strategy to extend the operation of brushless DC motors," in Proc. 2nd Int. Conf. Emerging Trends in Information Technology and Engineering (IC-ETITE), 2024, doi: 10.1109/IC-ETITE58242.2024.10493797.

[13] T. Shi, F. Zhao, H. Hao, and Z. Liu, "Costs, benefits and range: Application of lightweight technology in electric vehicles," SAE Technical Paper 2019-01-0724, Apr. 2019, doi: 10.4271/2019-01-0724.

[14] P. K. Mohanty, R. Pradhan, P. Jena, and N. P. Padhy, "Electric vehicles: Exploring types, benefits, challenges, policies, and smart charging innovation," in Electric Vehicle Charging Infrastructures and its Challenges, pp. 25–50, 2025, doi: 10.1007/978-981-96-0361-9_2.

[15] Business Wire, "E-bike market outlook & trends report 2025–2030, featuring Giant Manufacturing, Yadea, Pedego Electric Bikes, Merida, Trek Bicycle, Accell, Brompton Bicycle, Yamaha Motor, Pon.Bike & Aima Technology," Business Wire, Jan. 15, 2025. Accessed: Feb. 17, 2025. [Online]. Available: https://www.businesswire.com/news/home/20250115119173/en/E-BIKE-MARKET-OUTLOOK-TRENDS-2025-2030.

[16] F. Chai, Y. Bi, and L. Chen, "A comparison between axial and radial flux permanent magnet in-wheel motors for electric vehicle," in Proc. 2020 Int. Conf. Electrical Machines (ICEM), pp. 1685–1690, Aug. 2020, doi: 10.1109/ICEM49940.2020.9270905.

[17] C. Han, J. Y. Choi, and J. W. Yang, "Comparative analysis of axial and radial flux motors with identical size and output power," in Proc. 2024 Int. Conf. Electromagnetic Field Computation (CEFC), Jun. 2024, doi: 10.1109/CEFC61729.2024.10586086.

[18] T. Nguyen, J.-Y. Lee, and J.-H. Lee, "High power density axial-flux permanent magnet motor for electric bike application," IEEE Access, vol. 11, pp. 61621–61629, 2023, doi: 10.1109/ACCESS.2023.3281744.

[19] K. Ozer and M. Yilmaz, "Design and optimization of IPMSM for enhanced efficiency, cost reduction, and performance in light electric vehicles," IEEE Access, vol. 13, pp. 80621–80636, 2025, doi: 10.1109/ACCESS.2025.3567142.

[20] M. Naeimi, K. Abbaszadeh, and J. J. C. Gyselinck, "A novel external-rotor consequent-pole machine with asymmetrical and hybrid pole arrangement for e-bike application," IET Electr. Power Appl., vol. 19, no. 1, 2025, doi: 10.1049/elp2.70114.

[21] Q. Wang, C. Wang, and Y. Li, "Performance evaluating of rotor arrangement on high torque density in-wheel permanent magnet machines," IET Electr. Power Appl., vol. 17, no. 6, pp. 813–823, 2023, doi: 10.1049/elp2.12304.

[22] D. Mohanraj, R. Aruldavid, R. Verma, K. Sathiyasekar, A. B. Barnawi, B. Chokkalingam, and L. Mihet-Popa, "A review of BLDC motor: State of art, advanced control techniques, and applications," IEEE Access, vol. 10, pp. 54833–54869, 2022, doi: 10.1109/ACCESS.2022.3175011.

[23] Rahul, "Suzuki electric scooters & motorcycles to be launched in India by 2020," DriveSpark News. Accessed: May 24, 2025. [Online]. Available: https://www.drivespark.com/two-wheelers/2018/suzuki-electric-scooters-bikes

[24] C. Contò and N. Bianchi, "E-bike motor drive: A review of configurations and capabilities," Energies, vol. 16, no. 1, Art. no. 160, 2023, doi: 10.3390/en16010160.

[25] R. Rajamani, Vehicle Dynamics and Control. New York, NY, USA: Springer, 2012, doi: 10.1007/978-1-4614-1433-9.

[26] Z. Q. Zhu, D. Howe, E. Bolte, and B. Ackermann, "Instantaneous magnetic field distribution in brushless permanent magnet DC motors, Part I: Open-circuit field," IEEE Trans. Magn., vol. 29, no. 1, pp. 124–135, 1993, doi: 10.1109/20.195557.

[27] Y. Yokoi, T. Higuchi, and Y. Miyamoto, "General formulation of winding factor for fractional-slot concentrated winding design," IET Electr. Power Appl., vol. 10, no. 4, pp. 231–239, Apr. 2016, doi: 10.1049/IET-EPA.2015.0092.

[28] Z. Q. Zhu, D. Howe, and C. C. Chan, "Improved analytical model for predicting the magnetic field distribution in brushless permanent-magnet machines," IEEE Trans. Magn., vol. 38, no. 1, pp. 229–238, Jan. 2002, doi: 10.1109/20.990112.